Geophysical Journal International

Geophys. J. Int. (2015) **203,** 1847–1863
GJI Geodynamics and tectonics

doi: 10.1093/gji/ggv404

Integrating multidisciplinary, multiscale geological and geophysical data to image the Castrovillari fault (Northern Calabria, Italy)

F.R. Cinti,[1] C. Pauselli,[2] F. Livio,[3] M. Ercoli,[2] C.A. Brunori,[1] M.F. Ferrario,[3] R. Volpe,[2] R. Civico,[1] D. Pantosti,[1] S. Pinzi,[1] P.M. De Martini,[1] G. Ventura,[1,4] L. Alfonsi,[5] R. Gambillara[3] and A.M. Michetti[3]

[1] *Istituto Nazionale di Geofisica e Vulcanologia, Sezione Sismologia e Tettonofisica, Via di Vigna Murata* 605, *I*-00143 *Roma, Italy.*
E-mail: francesca.cinti@ingv.it
[2] *Dipartimento di Fisica e Geologia, Università degli Studi di Perugia, via Pascoli* 1, *I*-06123 *Perugia, Italy*
[3] *Dipartimento di Scienza e Alta Tecnologia, Università degli Studi dell'Insubria, Via Valleggio* 11, *I*-22100 *Como, Italy*
[4] *Istituto per l'Ambiente Marino Costiero, Consiglio Nazionale delle Ricerche, Calata Porta di Massa, I*-80133 *Napoli, Italy*
[5] *Istituto Nazionale di Geofisica e Vulcanologia, Sezione Geomagnetismo, Aeronomia e Geofisica Ambientale, Via di Vigna Murata* 605, *I*-00143 *Roma, Italy*

Accepted 2015 September 21. Received 2015 July 17; in original form 2014 December 31

SUMMARY

The Castrovillari scarps (Cfs) are located in northern Calabria (Italy) and consist of three main WSW-dipping fault scarps resulting from multiple rupture events. At the surface, these scarps are defined by multiple breaks in slope. Despite its near-surface complexity, the faults likely merge to form a single normal fault at about 200 m depth, which we refer to as the Castrovillari fault. We present the results of a multidisciplinary and multiscale study at a selected site of the Cfs with the aim to (i) characterize the geometry at the surface and at depth and (ii) obtain constraints on the fault slip history. We investigate the site by merging data from quantitative geomorphological analyses, electrical resistivity and ground penetrating radar surveys, and palaeoseismological trenching along a ∼40 m high scarp. The closely spaced investigations allow us to reconstruct the shallow stratigraphy, define the fault locations, and measure the faulted stratigraphic offsets down to 20 m depth. Despite the varying resolutions, each of the adopted approaches suggests the presence of sub-parallel fault planes below the scarps at approximately the same location. The merged datasets permit the evaluation of the fault array (along strike for 220 m within a 370-m-wide zone). The main fault zone consists of two closely spaced NW–SE striking fault planes in the upper portion of the scarp slope and another fault at the scarp foot. The 3-D image of the fault surfaces shows west to southwest dipping planes with values between 70° and 80°; the two closely spaced planes join at about 200 m below the surface. The 8-to-12-m-high upper fault, which shows the higher vertical displacements, accommodated most of the deformation during the Holocene. Results from the trenching analysis indicate a minimum slip per event of 0.6 m and a maximum short-term slip rate of 0.6 mm yr^{-1} for the Cf. The shallow subsurface imaging techniques are particularly helpful in evaluating the possible field uncertainties related to postfaulting modification by erosional/depositional/human processes, such as within stream valleys and urbanized zones.

Key words: Image processing; Tomography; Geomorphology; Palaeoseismology; Fractures and faults.

1 INTRODUCTION

The Castrovillari scarps (Cfs) are the surface expression of the Castrovillari fault (Cf; Cinti *et al.* 1997), a major normal seismogenic structure affecting the southwestern side of the Pollino Range (Calabria, southern Italy; Figs 1a and b).

Based on the available instrumental and historical seismic catalogues (ISIDe Working Group 2010; Rovida *et al.* 2011), the Pollino region represents a seismicity gap along the active axis of the Apennines, being an area where the occurrence of significant earthquakes ($>M6$) is infrequent or almost null. However, the available geological data (Bousquet 1973; Russo & Schiattarella 1992) and the palaeoseismological and archaeoseismological investigations (Cinti *et al.* 1997, 2002, 2015; Michetti *et al.* 1997, 2000) clearly show that the region contains active faults that produced large earthquakes in the past: one of these faults is the Cf. Historical catalogues do not

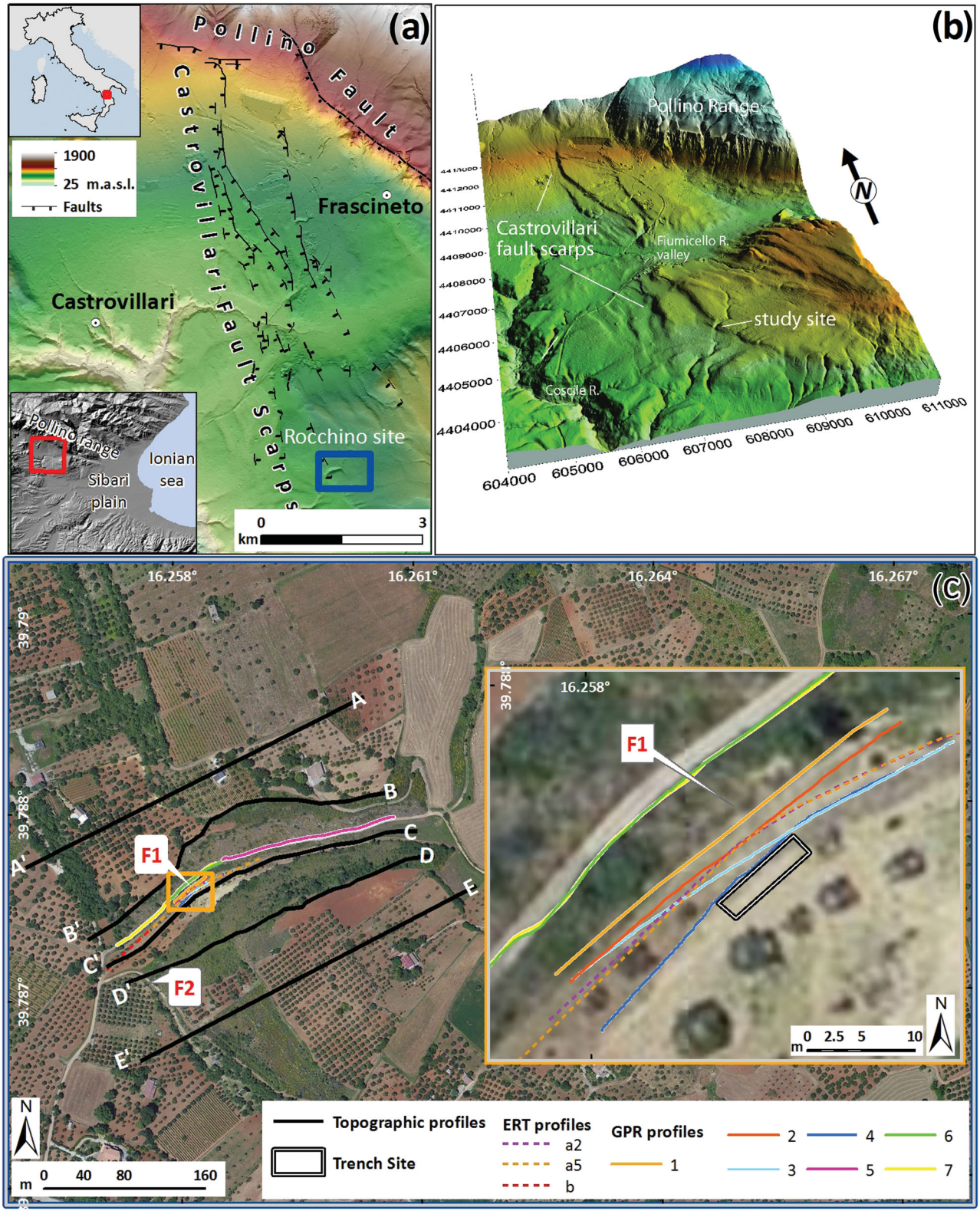

Figure 1. (a) Shaded relief (4-m pixel DEM) topographic map of the Castrovillari fault scarps (modified from Cinti *et al.* 2002). Blue box encloses the study site, referred as the Rocchino site. In the upper and lower insets, the study area is located within the red boxes. (b) 3-D topographic map (bird's-eye view from south) of the scarps area. (c) Esri satellite image showing the locations of various data profiles used in this study. F1 and F2 mark the locations of the two outcropping faults. The inset shows an expanded view of the area of acquisitions close to F1 zone (orange box). (d) Photo of the F1 outcrop and (e) photo of the F2 outcrop.

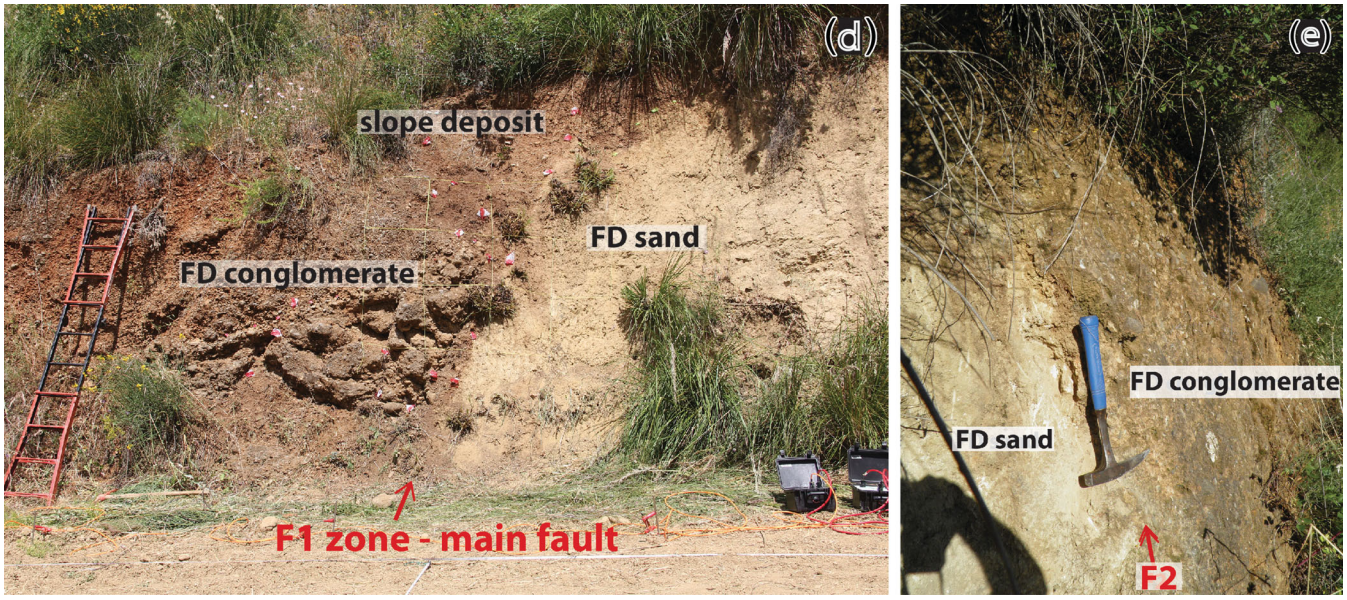

Figure 1. – (*Continued.*)

include large events in this area of Italy. Based on this apparent discrepancy, interest in the Pollino region has been is increasing, particularly since 2010 when the area was alarmed by a 3-yr earthquake sequence culminated with a $M = 5$ earthquake in October 2012. Therefore, an evaluation of the seismogenic potential of the region and of the Cf is of primary importance (e.g. Tertulliani & Cucci 2014).

The Cfs consists of three main WSW-dipping fault scarps that may have originated from separate rupture events along different fault splays. Antithetic, ENE-dipping scarps are also present and are responsible for the formation of local structural depressions. Despite its local complexity, the near-surface zone of deformation likely represents the geometry and the activity of a single seismogenic structure (Cinti *et al.* 2002, and reference therein). The scarp traces are parallel across a 1.5–2-km-wide zone, have an average strike of N150°, a length of 13 km, and are up to 40 m high. The Cf offsets multiple lithologies, including fan-delta, fluvial, lacustrine and colluvial deposits of middle to late Pleistocene and Holocene age, and Triassic to Lower Cretaceous limestone. The cumulative vertical throw of the fault scarps is about 90 m for the youngest top-set beds of the fan-delta sequence (broadly framed age 300–600 ka; Russo & Schiattarella 1992; Colella 1994), leading to a long-term vertical slip rate between 0.15 and 0.3 mm yr^{-1} (Cinti *et al.* 2002).

Taking advantage of recent developments in digital topographic mapping and new technologies for high-resolution shallow subsurface investigations, we conducted a new study on a selected site in the southern portion of the Cfs system (Figs 1a and b).

The objectives of this study are: (i) to image the 2-D and 3-D Cf surface and subsurface geometry by integrating data from four techniques of investigation: quantitative geomorphological analysis, electrical resistivity (ERT) surveys, ground penetrating radar (GPR) surveys and palaeoseismological trenching (Fig. 1c); (ii) to evaluate the geometry and slip history of the fault zone by multiple analyses of independent Cf images; (iii) to evaluate methods for the visualization and characterization of active faults in comparable tectonic environments.

2 THE STUDY SITE

We selected a site, hereinafter referred as Rocchino site, along one of the southern scarps of the Castrovillari scarp system. The site is located at about 6 km SE of Castrovillari city (Figs 1a–c) and was chosen because of (a) the presence of Holocene soft alluvial sediments that may have recorded deformation from recent earthquakes, (b) it was particularly suitable for multiple evaluation techniques and (c) it was easily accessible for the planned geophysical techniques and for palaeoseismological excavations. In addition, the Rocchino site is located along a scarp portion of the Cfs system that has not been previously investigated.

At the Rocchino site, the Castrovillari scarp has created a NNW–SSE (locally N150°) striking, 30-m-high scarp. This scarp consists of alternating thick sand and silt packages, strongly cemented conglomerates, and coarser gravels. The age of the deposits is generally assigned to the Middle–Late Pleistocene (Carta Geologica d'Italia, 1:50 000, Foglio 534), and it is part of the youngest phase of deposition of the Plio–Pleistocene fan delta sequence in the area.

The scarp is transversally crossed and deeply eroded by a stream incision, and within the valley floor, its expression is a gentle inflection in the late Holocene alluvial deposits. The current setting of the valley partly results from human modifications (road cut half way along the slope, retreat of the natural edge to obtain a wider cultivable land).

The Cf planes are exposed at two distinct locations. The best outcrop is that of the fault zone 1 (F1), at the northern valley edge (Figs 1b–d). The F1 zone is aligned with an inflection within the valley floor and corresponds to a sharp slope change along and parallel to the scarp relief. The main fault trace within this zone strikes N160°, and dips 70°. This fault vertically displaces (W–SW side down) fan delta deposits (FD) and slope colluvium. Another fault, 2 (F2), is exposed at the base of the escarpment (Figs 1c and e), and it juxtaposes conglomerate and sand of the fan delta sequence.

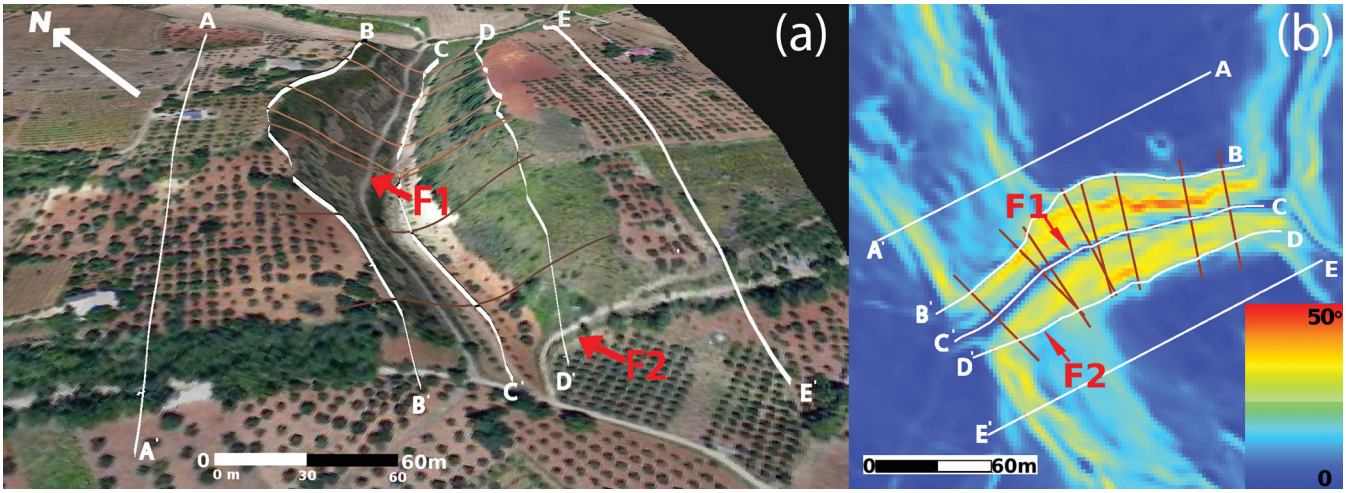

Figure 2. (a) Esri images with topographic profiles at the Rocchino site (AA′ to EE′, shown in Fig. 3; see Fig. 1 for site location). The thin brown lines are included to highlight the shape of the valley. F1 and F2 refer to the location of the fault outcrops (see also Figs 1d, e). (b) Slope map of the site with the trace of the longitudinal profiles (AA′–EE′) and the lines transverse to the valley [brown lines as in (a)].

3 *IN SITU* ANALYSIS

3.1 Geomorphological scarp analysis

We conducted a detailed morphological analysis using a 4 × 4 pixel DEM (C.T.R.-Carta Tecnica Regionale acquired in 2014 from the Ufficio Cartografico, Calabria Region), which has been used to produce shaded relief and slope maps (e.g. Brunori *et al.* 2013). The DEM analysis was also supported by interpretation of aerial images (ESRI-World_Imagery) and by a field survey, to help the discrimination between natural and man-made features.

We evaluated five profiles (AA′–EE′, from north to south) that cross the fault scarps (Figs 1c and 2). Profiles AA′ and EE′ are outside of the stream valley, whereas profiles BB′–DD′ and CC′ are at the top of the flanks and within the central portion of the valley, respectively. Profiles BB′ and DD′ are along the intercection between the lateral erosional surface of the stream and the ridge slope; that is why they are divergent from the other rectilinear traces (AA′ and EE′).

Based on the scarp slope geometries and the locations of the F1 and F2 exposures relative to the slope (Figs 1c and 2), we identify multiple breaks in slope, generally marking the boundary between upper scarp degradation and lower debris accumulation. These slope breaks approximately mark the intersection of fault planes and slope surface (Fig. 3).

On the basis of slope inflections, southwest side down, we infer four fault planes that are generally consistent with the fault geometry interpreted for the area. Our interpreted fault locations are accurate to within ±2 m horizontally, according to the DEM data. We differentiate the faults such that the topographically higher fault planes are in black, green, red and blue. The green and the red planes (∼20 m apart) are referred as the F1 zone and the blue as the F2 (Fig. 3); these planes are observed in the field close to profiles BB′ and DD′ (Figs 1c–e).

The surface offset relative to the F1 zone ranges between 8 and 10 m (δf1, profile AA′ in Fig. 3). An offset of about 8 m is associated to F2 at the foot of the scarp (δf2, profile AA′ in Fig. 3). These values are quite consistent in AA′–BB′–DD′–EE′. Due to the gully erosion and the anthropic modifications, the individual scarps within the valley floor (profile CC′ in Fig. 3) are removed or their height is reduced; in particular, the smoothed scarp associated with fault zone F1 is about 2 m high (Fig. 3).

At the Rocchino site, the cumulative fault slip created the local Cfs ridge slope, that is about 40 m high (δfs, profile AA′ of Fig. 3), with a N145° strike and dip values ranging from 10° to 20°. Based on the total (40 m) height of the scarp and the maximum age of the fan-delta surface (Late Pleistocene, 126 Ka), we estimate a minimum long-term slip-rate of ∼0.3 mm yr^{-1}, a value consistent with that calculated by Cinti *et al.* (2002).

The slip on F1 is Holocene and has influenced the stream valley morphology. As highlighted by the brown lines in Fig. 2, the valley's morphology, and the direction sharply change at the relative interception with F1.

3.2 ERT survey

We conducted three tomographic ERT surveys within the gully floor at the Rocchino Site (ERTa5; ERTa2 and ERTb—see Fig. 1c for location). Data acquisitions are geo-referenced and topographically corrected with sub-cm vertical accuracy, using a total station. The sections were acquired using a PASI® (mod. 16GS32) instrument, consisting of the following set-up: PC-resistometer, charged by a 12V–45A battery; 32 steel pikes for voltage measurement divided into two sets of 16 pikes, each connected by two isolated cables and through two link-boxes to a booster. We acquired the tomographic lines using electrode spacing of 2 and 5 m, varying with the target depth. We processed the signal using the Res2DInV software (Ver. 3.55). To detect both horizontal and vertical subsurface structures, we acquired the sections with varying arrays: dipole–dipole, Wenner and Wenner–Schlumberger (WS). Each of the arrays has specific advantages and/or limitations with respect to: (i) directional sensitivity, (ii) absolute signal/noise ratio, (iii) depth of investigation and (iv) geometry of the coverage area (Loke 2011).

In particular, the Wenner array is relatively sensitive to vertical changes in the subsurface resistivity, especially below the centre of the array but less sensitive to horizontal changes. Among the common arrays, the Wenner array has the strongest signal strength, and this can be an important factor if the survey is carried out in areas with high background noise.

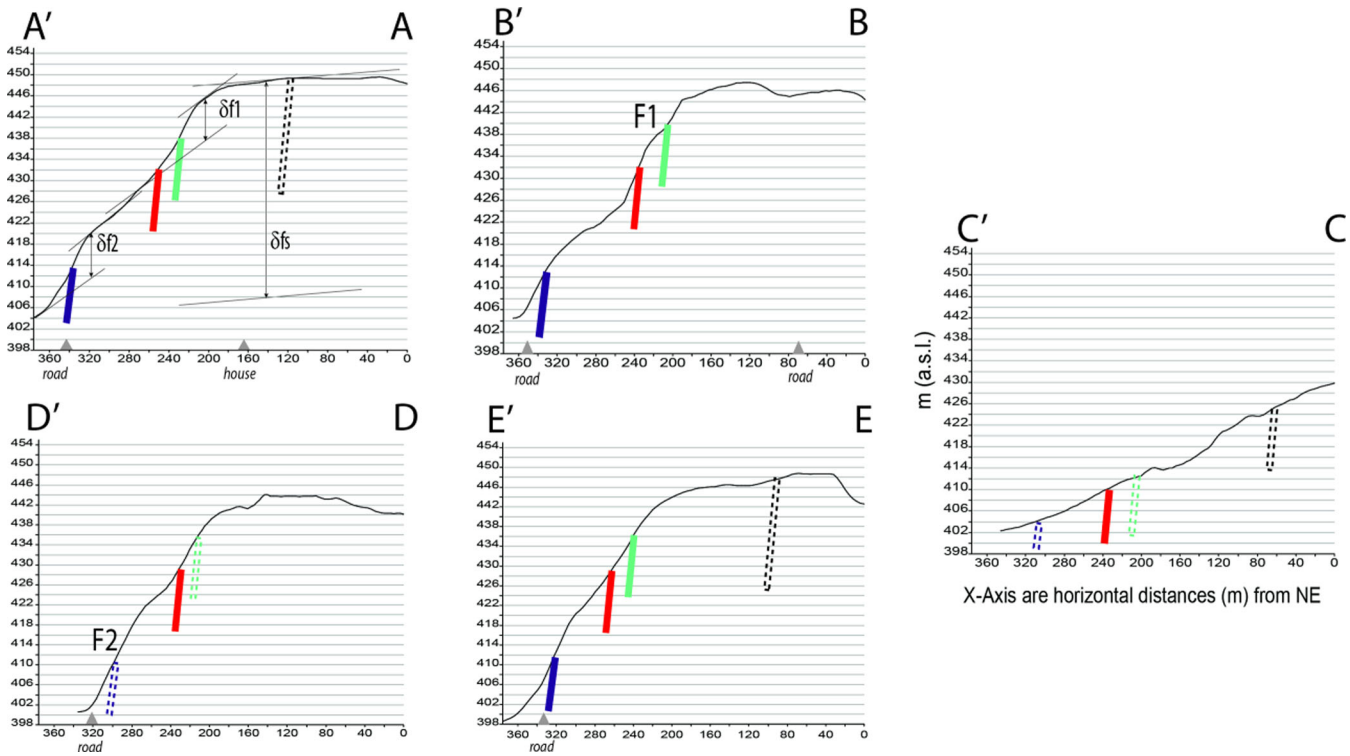

Figure 3. Topographic profiles across the Cfs at the Rocchino site (AA′–EE′, see Fig. 1c and 2 for location of traces). Vertical exaggeration is 5. Locations of manmade structures along the profiles are marked with grey triangles on the *X*-axis. Black, green, red and blue lines are the locations of the inferred fault planes, dashed where uncertain. The red and green lines are referred as F1 zone, and the blue lines F2. Exposures of these faults are observed along profiles BB′ and DD′, respectively (see also Figs 1c and d). Vertical separation across the faults is inferred. A correlation between displaced slope surfaces is graphically shown in profile AA′ (δf1 across F1 zone, δf2 across F2 and δfs across the entire scarp).

Table 1. Acquisition parameters of the ERT. *W, Wenner; D, dipole–dipole; S, Wenner–Schlumberger.

Section #	Electrode distance (m)	Array (*)	Length (m)	Figure
ERTa5	5	W;D;S	155	4
ERTa2	2	W;D;S	62	5
ERTb	2	D;S	62	6

The dipole–dipole array, on the other hand, is sensitive to horizontal changes in resistivity, but relatively insensitive to vertical changes. In general, this array has a shallower depth of investigation compared to the Wenner array, but due to the vertically consistent pattern of the sensitivity contours, the depth of investigation is not particularly meaningful for the dipole–dipole array. One possible disadvantage of this array is the low signal-to-noise ratio.

The WS array has a slightly better horizontal resolution compared with the Wenner array. The horizontal data coverage is slightly wider than the Wenner array, but narrower than that obtained with the dipole–dipole array. Vertical versus horizontal sensitivity for the WS array is intermediate between the Wenner and dipole–dipole arrays.

We used all the three aforementioned arrays to detect both horizontal and vertical changes in resistivity and thus, to infer a final section interpretation, differentially weighting the geometrical constraints of each array.

Two sections, ERTa5 and ERTa2 (Table 1), were centred on the outcropping fault zone F1. The 5-m-spaced-line, ERTa5, allowed us to investigate the subsurface down to ∼25 m depth (Fig. 4); the more detailed 2-m-spaced-line imaged to ∼12 m depth (Fig. 5).

We acquired Section ERTb (Table 1 and Fig. 6) within the gully on the western end of the ERTa5 line, where the F2 fault projection is expected (Fig. 1c).

The outcrops at the edge of the gully expose lithology that is characterized by a sequence of alternating conglomerates and sands, which are of high and relatively low resistivity values, respectively. In the following, resistivity units, labelled with capital letters (A, B, C, etc.), are described for each section, based on the contrast between adjacent areas and consistency with outcropping sediments and GPR data (*cf.* Section 3.3). Generally, abrupt near-vertical lateral changes in the resistivity can be interpreted as tectonic contacts. There are also lateral stratigraphic changes. On each ERT section, we labelled resistivity units using capital letters from the upper to the lowermost. Finally, we integrated all the constraints based on our interpretation of the varying arrays into an interpreted geological model with stratigraphic units that are observed in all the three sections; stratigraphic units are indicated by a progressive numbering, from the bottom to the top.

ERTa5 line

The ERTa5 line was acquired with the Wenner array (Fig. 4a). Along the NE side of the section, between 85 and 140 m, a low-resistivity tabular body (B), ∼5 m thick, overlies high resistivity units (D). These bodies, gently dipping to the SW, abruptly die out westward against a tabular body of medium-to-high resistivity units that is about 5 m thick (A), with an underlying complex pattern of slightly lower resistivity bodies (C). The westward termination of B and D infers a subvertical contact, apparently dipping to the SW (∼75°). This significant horizontal resistivity change occurs along the F1

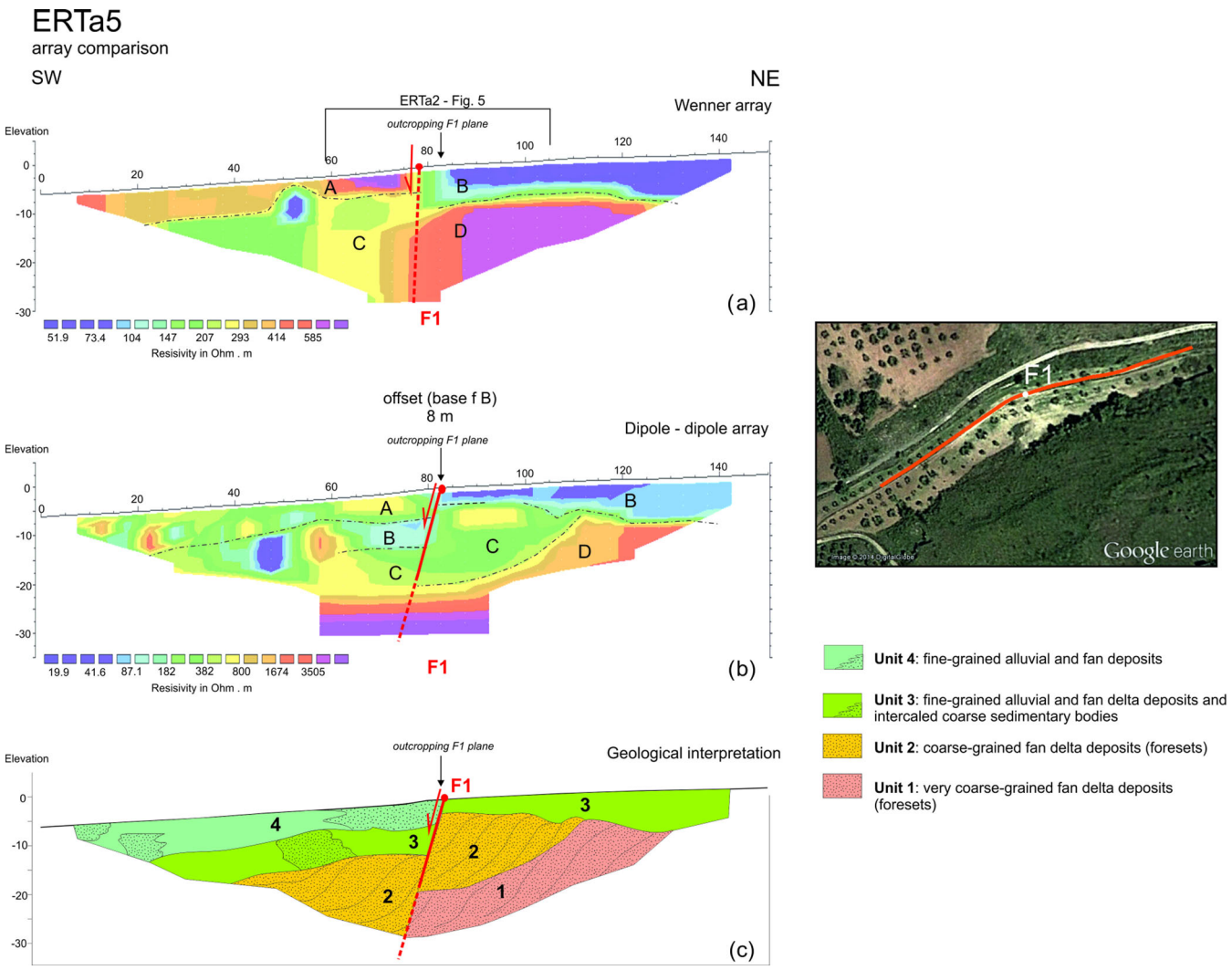

Figure 4. ERTa5 section (Fig. 1c for location). (a) Wenner. (b) Dipole–dipole array. (c) Geological interpretation. Resistivity units are indicated with capital letters, whereas the inferred stratigraphic units on the geological model are indicated by progressive numbering. Red lines are the interpreted fault zones (dashed when uncertain), and the red dot marks the surface location of the observed fault plane.

fault zone in outcrop, and we interpret the resistivity change as the continuation of the F1 zone at depth, here imaged as a ∼10-m-wide zone. Given this wide lateral change in resistivity, the fault dip angle cannot be clearly interpreted; moreover, no correlative bodies are observed along this array, and consequently, no displacement can be estimated for F1. The overall geometry of the stratigraphic bodies can be inferred in spite of the complex stratigraphic architecture of the site. The Wenner array suggests that the fault plane extends down to the bottom of the section (∼25 m below ground level).

A deeper inspection on the fault geometry and a vertical offset can be inferred from the dipole–dipole configuration (Fig. 4b), whereby shallow geometries, mean thicknesses and resistivity values, as observed in the Wenner array, can be observed as well. Two tabular shallow units (A and B) are separated by a high-angle SW-dipping zone, which we interpret as F1. The high-resistivity body underlying B in the fault footwall is separated into a deeper high-resistivity zone (D), passing upward through a moderately SW-dipping surface to a lower resistivity body (C). This pattern, consistent with other data from GPR surveys (*cf.* Par.3.3), suggests that D and C can be interpreted as a package of southwestward dipping foresets, probably composed of fining-upward alluvial fan deposits. In the hangingwall section of the line (0–85 m) a shallow medium-resistant unit (A) overlies low and high resistivity zones (B), possibly correlating with the same sector imaged in the footwall sector. This unit, in turn, overlies a continuous medium-resistivity body (C), correlative with the same units in the footwall.

Fault geometry is here better imaged (located at ∼82 m along the section), with a SW-dipping (∼80°) fault plane that correlates at the surface with the F1 outcrop. We estimate a cumulative vertical offset of ∼8 m on the basis of the location of the base of unit B across the inferred fault plane (Fig. 4b).

Our geological interpretation of this section combines constraints from each array: we infer four stratigraphic units (Unit 1–4) that are consistent with the resistivity units. Our interpreted average depth of each sedimentary unit and the maximum depth of the fault plane are based on data from the Wenner array, whereby we deduced complex lateral changes in the sedimentary bodies, fault dip angle, and offset from dipole–dipole array.

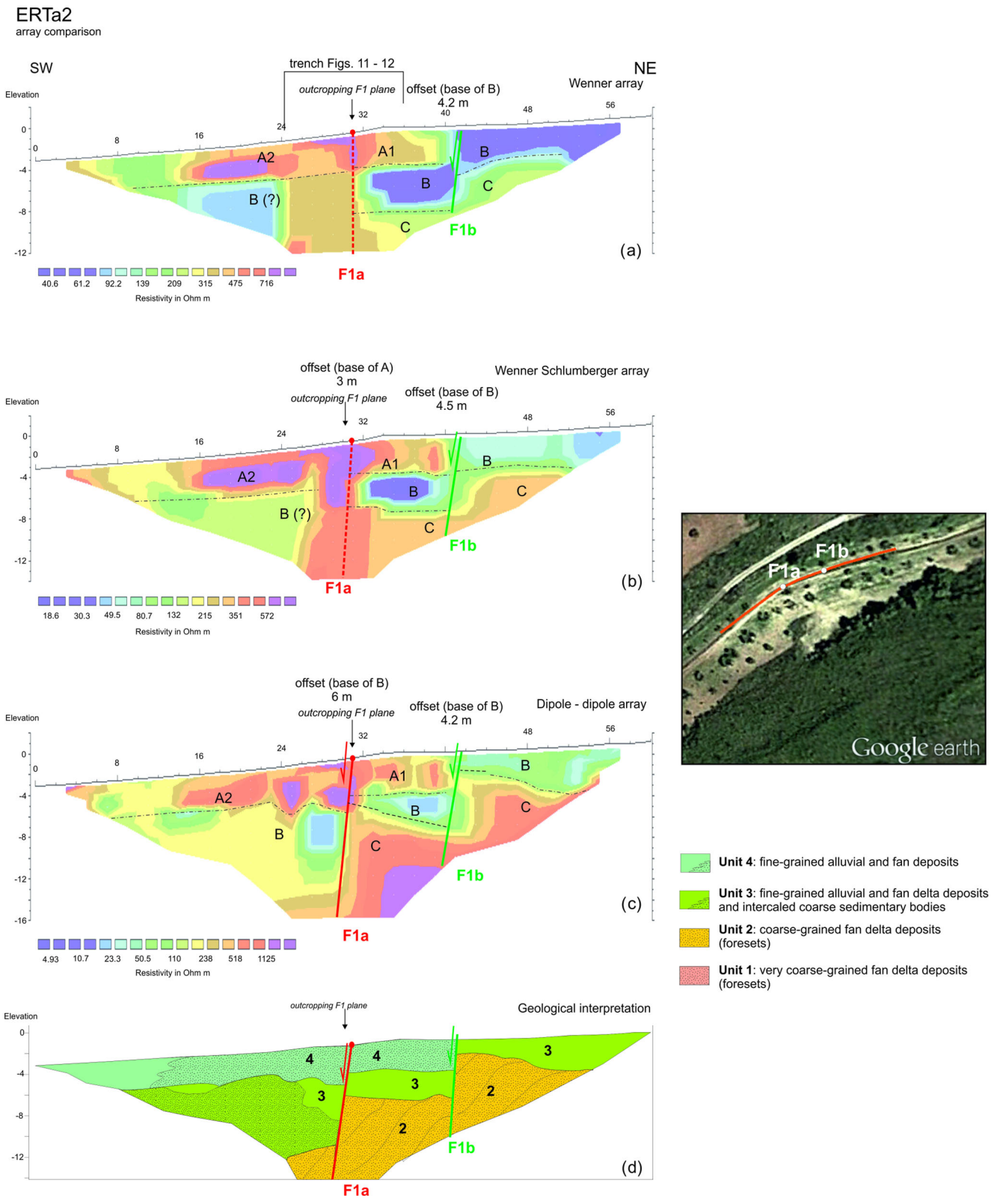

Figure 5. ERTa2 section (Fig. 1c for location). (a) Wenner. (b) Wenner–Schlumberger. (c) dipole–dipole arrays. (d) Geological interpretation. Resistivity units are indicated with capital letters, whereas the inferred stratigraphic units of the geological model are indicated by progressive numbering. Red/Green lines are the interpreted fault zones (dashed when uncertain), and the red dot marks the surface location of the observed fault plane.

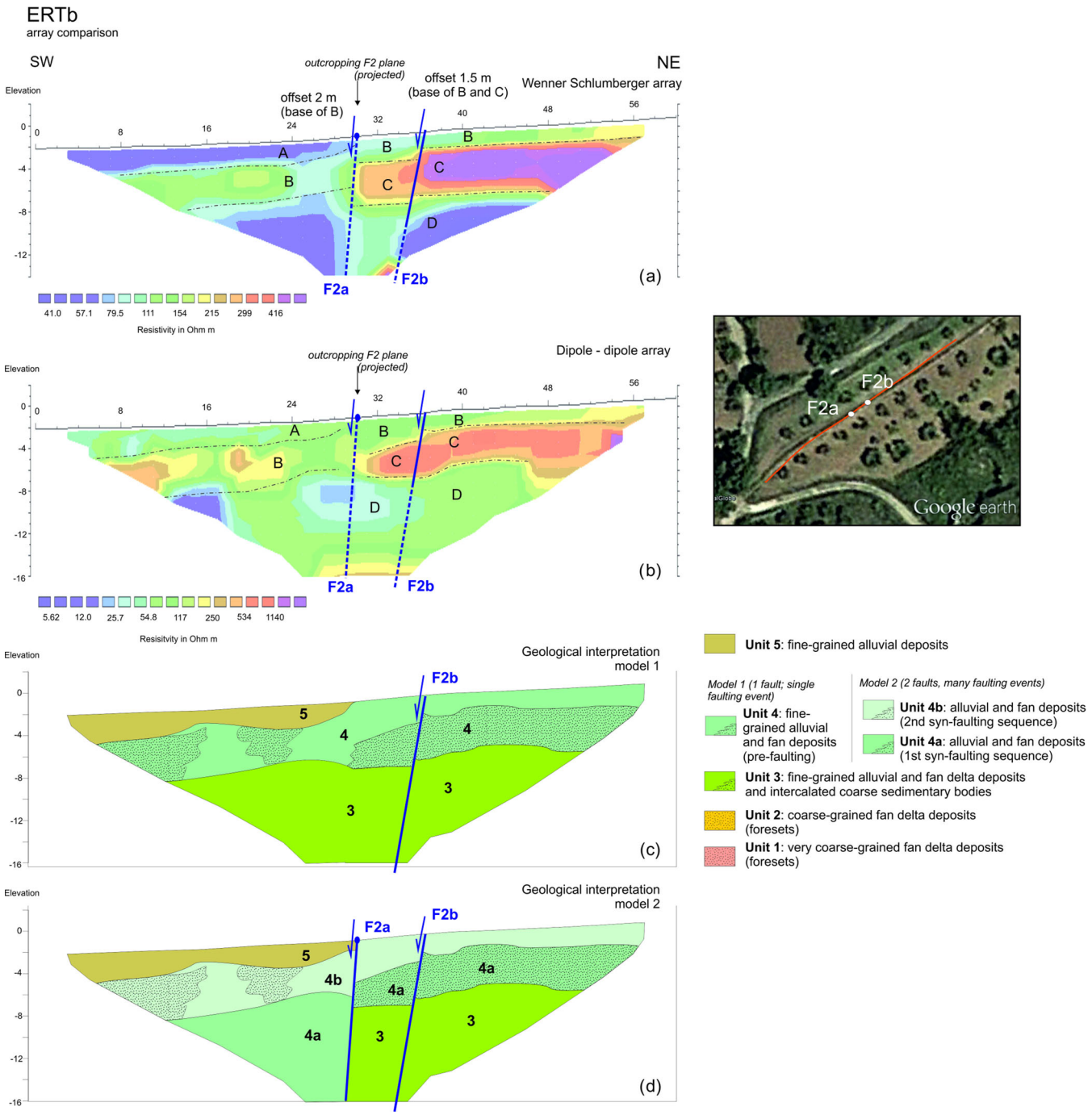

Figure 6. ERTb section (Fig. 1c for location). (a) Wenner–Schlumberger array. (b) dipole–dipole array. (c) Geological interpretation—Model 1. (d) geological interpretation—Model 2. Resistivity units are indicated with capital letters, whereas the inferred stratigraphic units on the geological model are indicated by progressive numbering. Blue lines are the interpreted fault zones (dashed when uncertain), and the blue dot marks the projection on the section of the nearby observed fault plane.

ERTa2 line

ERTa2 was centred on the projection of the F1 zone as seen in outcrop, and it overlapped ERTa5 trace (Fig. 1c) so that the area was imaged with two different array spacings. Along ERTa2 (Fig. 5), the horizontal changes in the resistivity suggest the presence of two distinct fault planes, likely belonging to F1 fault zone. The overall resistivity distribution observed from the two arrays is similar. The NE section of the profile contains a low-resistivity unit that overlies a slightly higher-resistivity unit (C). Unit B is displaced along a high-angle surface, interpreted as a fault plane (F1b). Vertical offset can be estimated on all three arrays, resulting in similar values (~4.3 m). F1b dips to the SW on all the sections (~80° of dip angle).

The three arrays differ considerably in the central and SW part of the profile, where the F1a hangingwall and fault zone are located. Both Wenner and WS arrays display evidence for the F1a fault zone, whose location at the surface is constrained in outcrop at the valley edge as a relatively high-resistivity subvertical structure that is 4–8 m wide. The F1a geometry and vertical offsets of stratigraphic units are not determined from the Wenner and WS arrays. Units A1

Table 2. Acquisition parameters used during the survey for the GPR profiles.

Profile #	Operative frequency (MHz)	Profile length (m)	Trace length (ns)	Samples per trace (n°)	Trace distance (m)	Vertical stacking (n° traces)
GPR1	300	38	100	512	0.01	5
GPR2	300; 500	38.5	200; 100	512	0.05; 0.01	5 (only on 500 MHz data)
GPR3	300	41.5	200	512	0.05	–
GPR4	300	43	200	512	0.05	–
GPR5	500	163	200	1024	0.01	5
GPR6	300; 500	70	200	1024	0.01	5
GPR7	300	129	200	1024	0.05	5

and A2 (resistivity units seem correlative) are not clearly displaced nor are they well imaged in the profiles; a small displacement can be inferred at the base of these units as recorded on the WS array (Fig. 5b). The dipole–dipole array (Fig. 5c) offers more details on the geometry of the fault zone. The dip angle of both the fault zones can be inferred by this array; moreover, a low-resistivity body can be inferred in B unit, close to the F1a plane and correlative with the B unit in the footwall sector, thus allowing the measurement of fault offset (∼6 m).

Based on the dipole–dipole and WS arrays, we infer the offset across F1a to be ∼3 m, at the base of Unit A and ∼6 m at the base of Unit B; and that of F1b to be ∼4.3 m measured at the base of Unit B (Figs 5b and c). It is noteworthy that the total cumulative offset measured on these two faults, is consistent with that measured on the single fault zone imaged in the ERTa5 section.

Our interpreted geological model consists of three of the same stratigraphic units (Unit 2–4) observed in the section ERTa5.

ERTb line

The ERTb section has an electrode spacing of 2 m and the line is centred along the hypothetical projection of the F2 outcrop (Fig. 1c). In both the WS (Fig. 6a) and dipole–dipole (Fig. 6b) sections a shallow high-resistivity zone, ∼8 m thick, is present in the NE sector of the profile (C in Fig. 6), and is overlaid by a thin low-resistivity body (B) that thickens, to the SW. Finally, at the bottom of the section we infer a low-resistivity unit (D).

Unit C abruptly discontinues to the SW at 30 m distance along the profile, where we traced the projection of F2 fault zone. However, no correlative unit to C is recognized farther to the SW. In addition, unit B shows a major step at this point, with the downthrown side to the SW. The Wenner array displays a subvertical zone of relatively higher resistivity (∼100 Ω m) down to the bottom of the section, separating two adjacent lower-resistivity zones (∼40 Ω m), as also observed in the ERTa sections, at the F1 fault zone. We interpret this as indicative of a fault zone (F2a) probably dipping to the SW, as suggested by the discontinuous nature of unit C observed from the Wenner array and consistent with both geomorphological observations (see Section 3.1) and the nearby outcropping F2.

Conversely, the lack of the correlative unit C in the downthrown block and the apparently continuous unit D body, as imaged by the dipole–dipole array, could be explained by lateral *facies* changes of the alluvial and fan delta bodies, thus implying the absence of a fault zone.

The bases of unit B and unit C appear to be slightly displaced by the same amount of vertical offset (∼1.5 m) on both the arrays at a distance of ∼35 m. We interpreted this as a secondary fault trace (F2b) which moved after the deposition of unit C.

Two possible geological models can thus be invoked for the interpretation of section ERTb (Fig. 6) after taking into account all the evidence and uncertainties discussed above. Model 1 (Fig. 6c) includes a single fault, whereas model 2 (Fig. 6d) includes a major fault zone (F2a) with vertical offset progressively increasing downward from ∼2 m at the base of Unit 4b to more than 10 m at the base of unit 4a.

3.3 Ground penetration radar survey

2-D GPR is an efficient tool for the study of geological discontinuities like faults and fractures and for the characterization of the related sedimentary structures (Liner & Liner 1997; Jewell & Bristow 2006; Vanneste *et al.* 2008; Christie *et al.* 2009; McClymont *et al.* 2010; Pauselli *et al.* 2010; Carpentier *et al.* 2012; Ercoli *et al.* 2013).

A GPR dataset was recorded using a Zond 12e GPR unit integrated with a TopCon GR5 Global Navigation Satellite System (GNSS) and a real-time NRTK connection (NetGEO, courtesy of Geotop S.r.l.), which allowed us to georeference GPR traces during acquisition, and to provide accurate locations (∼cm accuracy; WGS 84 UTM33 coordinates). We acquired our data in dry conditions. In addition, the characteristics of the site are ideal for GPR acquisition along our study areas. The stratigraphic sequence is mainly composed of fan-delta deposits that do not include clays that could attenuate the electromagnetic signal; however, conductive clay may have been present in the middle portion of the road (alluvial/colluvial deposits, a strong attenuation was observed during preliminary tests). Moreover, metal structures, which may interfere with the GPR signal, were not present in our study area. About 800 m of 2-D GPR data were recorded using several antennae, among which the 300 MHz and 500 MHz were used to exploit different resolution capabilities and depth of investigation (Jol 2009). Here, we present only the profiles that are most important in demonstrating faulting relationships. Our data consisted of a maximum of 1024 samples in time windows ranging from 50 to 300 ns, and our trace spacing varied from 1 to 5 cm, depending on the operative frequencies used. The acquisition parameters used during the survey are summarized in Table 2.

Frequency pass-band filters were used to remove undesired high and low frequency noise components (DC-shift and environmental noise) and an amplitude recovery function was used to to recover the true amplitudes, attenuated in the raw data due to propagation and attenuation effects. An average velocity value of 0.095 m ns^{-1}, corresponding to a relative permittivity of 10, is estimated through a hyperbolic diffraction analysis. This value has been used for the time to depth conversion of the GPR profiles and for *f–k* migration applied together with an accurate topographic (static) correction. Fig. 7 shows examples of fully processed profiles.

The 300 MHz GPR1 and GPR2 profiles, acquired in a NE–SW direction along the valley floor close to the F1 outcrop visible in Figs 1(c) and (d) are the most informative: after multiple tests, the 300 MHz frequency data show the best compromise between

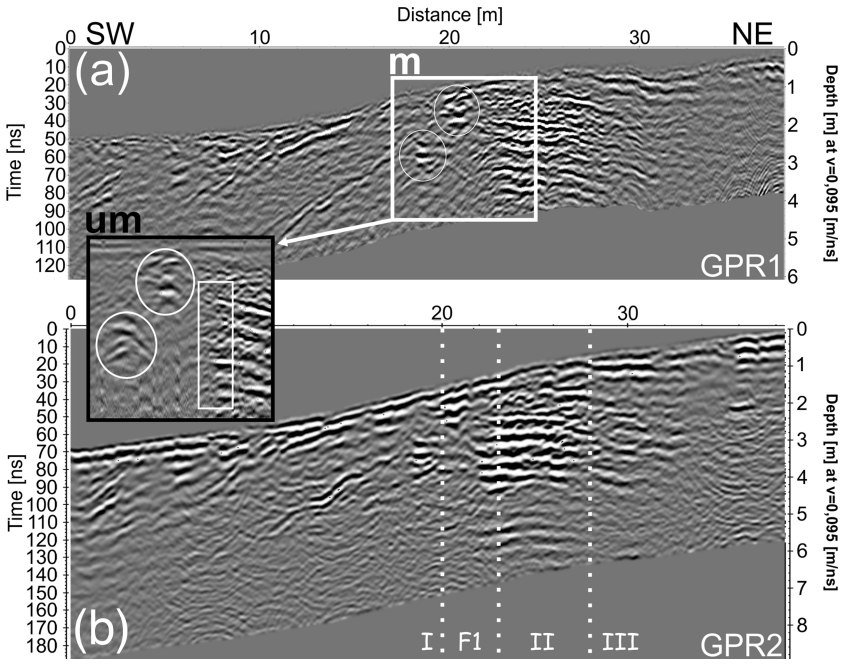

Figure 7. Fully processed profiles. (a) GPR1 and (b) GPR2. The black square encloses the unmigrated version (um = unmigrated) of the profile highlighted in the white box (m: migrated), showing the discontinuous lateral reflectors and the presence of diffractions. Vertical exaggeration is 2.

penetration depth and resolution for the geological characteristics of the profiles, showing a better S/N ratio (Fig. 7a). The radargrams can be divided into four sectors having varying geophysical characteristics: between 0 and 20 m, W–SW dipping reflectors are dominant (zone I in Fig. 7b); between 20 and 23 m, the peculiar radar signatures indicate the presence of a fault zone (F1). Some diffraction hyperbolas (unmigrated radargrams, e.g. in the black square in Fig. 7b), a focused and strong amplitude decrease along the fault 'plane', and laterally discontinuous reflectors are observed in the data (for details, see Ercoli *et al.* 2013). In zone II between 23 and 28 m gently NE dipping reflectors are characterized by strong reflectivity, whereas between 28 and 38 m some weaker reflections are localized in zone III (Fig. 7a).

The reflectors in zone I may represent the fan delta sedimentary bodies of deposition cycles, which are presently exposed in outcrops along the valley (Fig. 1d). The reflectors in zone III and on the top part of zone II (Fig. 7a) can be correlated with the nearby outcropping ochre fine sands/silts (Fig. 1d) and may characterize another probable fault further more to NE (Fig. 8, green dashed line). The high-amplitude reflectors in zone II probably result from a 'highly cemented sedimentary unit' located at about 1 m depth.

To enhance the detection of lateral discontinuities like fractures and fault zones, the processed data were also evaluated with an attribute analysis, calculating and successively mixing instantaneous amplitude attributes (GPR trace envelope) and phase attributes (e.g. cosine of instantaneous phase; Zhao *et al.* 2013). In Fig. 8(a) the instantaneous amplitude profile was overlapped on the same fully processed radargram, whereas Fig. 8(b) shows the cosine-phase attribute merged with the instantaneous amplitude. In all the GPR profiles, we interpret fault zones as areas of high signal attenuation, abrupt lateral variation in amplitude, and zones of discontinuous reflectors (e.g. Ercoli *et al.* 2014).

For the GPR2 profile, we observe two main, closely-spaced fault 'zones', labelled as F1 zone, (red, F1a and green, F1b, dashed lines). These two features are also surrounded by several smaller discontinuities observable at centimetric scale.

GPR7 and GPR5 are shown in Fig. 9. In Fig. 9 both the processed images obtained by superimposing the attributes were reported to highlight the interruptions of the layers. These profiles were acquired to extend the detailed observations seen along the F1 zone. The fully processed profiles highlight the presence of others fault traces and a dominant SW dip of the sedimentary units seen in the GPR1 and GPR2 (zone I).

All the georeferenced 2-D GPR sections were uploaded onto a Free and Open Source interpretation software package (OpendTect, dGB Earth Sciences) to develop a 3-D reconstruction of the shallow geological setting of the study site.

The final interpretation was done first by locating all the possible fault traces based on the GPR fault-signatures illustrated above, then by developing a 3-D perspective (Fig. 10). The dip direction of the fault planes within the fault zone is usually not easily determined using traditional interpretation techniques. The combined use of basic amplitude and phase attributes can greatly enhance interpretation. The dip angles of the faults have been reconstructed by interpolating the phase discontinuity and truncations of layers, along with lateral variations in amplitude and attenuation. The dip of the main fault plane (red) on F1a is inferred to be about 70°, whereas an estimation of the vertical offset cannot be determined due to attenuation within the hanging wall of the fault, located in the SW sector of the radargrams (Fig. 8). In fact, the strong reflectors located within zone II, close to F1, are not detectable at depth inside the radargrams, suggesting a throw for these layers higher than 4 m. Our interpretation of this GPR dataset suggests that the total slip associated with this fault strand may be distributed over a wider fault zone, as suggested by the opposite and gently NE-dipping layers located between the red (F1a) and the shallower dipping green (F1b) strands located about 15 m eastward (Fig. 8). An estimate of the dip and fault offset is complicated by the weak reflections resulting from higher attenuation and a lower S/N ratio. An additional fault strand can be inferred within the GPR5 profile at about 105 m along the line (black dashed line F3 in Fig. 9d). This strand is characterized by a small topographic scarp (less than 1 m) on the surface,

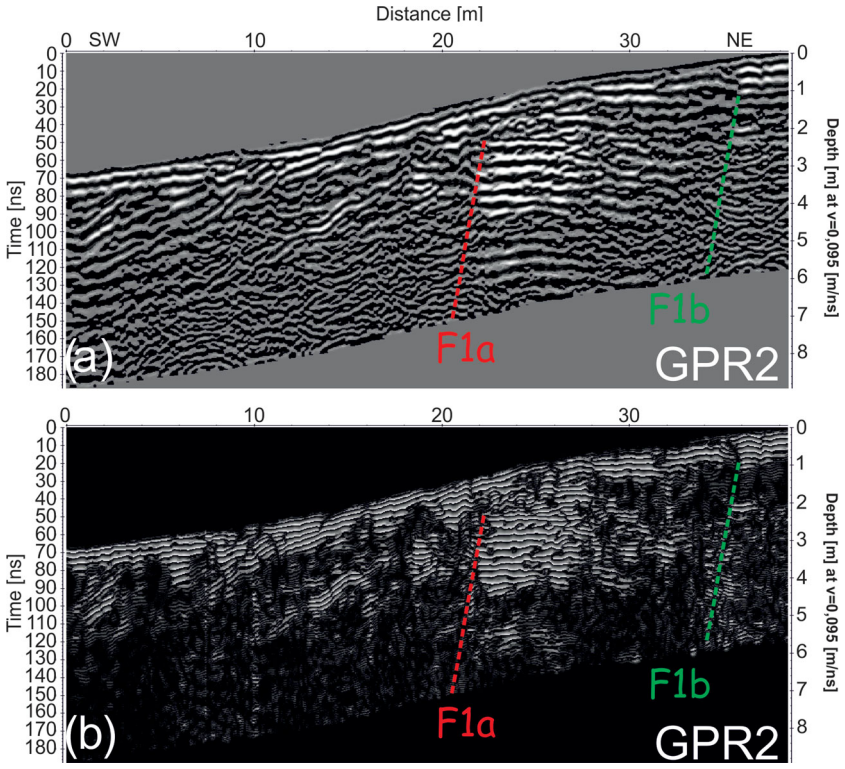

Figure 8. Processed profile GPR2. (a) Fully processed profile visualized together with the envelope attribute. (b) Phase attribute overlapped on the envelope. The red and green dashed lines mark the interpreted fault strands belonging to F1 and emphasized by the attributes visualizations. Vertical exaggeration is 2.

by a narrower fault zone with focused GPR signal attenuation and by the lateral interruption of the hanging-wall layers, that abruptly change angle (higher dip) close to fault zone. We estimate the dip to be about 70°, whereas the total vertical offset is calculated to be less than 0.40 m. The GPR5 profile highlights the general SW-dip of the layers, showing continuity all along the profile. The highly attenuated zone between about 78 and 84 m (Fig. 9c) has not been interpreted as a fault zone. The SW-dipping layers show an overall continuity despite the strong attenuation, probably originated by the strong reflector located in the shallowest layers. Finally, the portion of the profile between 0 and 60 m is highly attenuated. It shows very low amplitudes below the first 2 m of depth, probably due to the presence of conductive units. Therefore, we have not inferred the presence of additional fault splays in our final interpretation.

3.4 Palaeoseismological trenching

We excavated the scarp within the valley floor along the projection of the F1 zone (Figs 1c,d and 11). Here, although the scarp is reduced to a gentle inflection because of erosion, it was possible to acquire fault slip history data from the alluvial deposits (see also Section 2).

The subsurface imaging from the geophysical campaign guided the trench positioning, and in particular the ERTa (Figs 4 and 5) and GPR1 to GPR4 (Figs 7 and 8) sections pointed to the F1 zone below the ground inflection, to the right edge of the valley and to the deepening of the floor (see Sections 3.2 and 3.3 for details).

The trench was dug about 6 m from the northern edge of the valley (Fig. 11): trench walls direction N40°–N50°, length 13 m, and max depth 3 m.

The stratigraphy consists of a strongly cemented conglomerate (FD), that is the oldest unit exposed, and a succession of alluvium and colluvium deposits (AC, silt, clayey silt, conglomerate and gravel; Fig. 12). The reworked portion (R) of the ground surface is quite thick, reaching 1 m. There is a clear correlation between the stratigraphic units along both trench walls. The southern wall exposes a larger thickness of the young deposits filling the valley (AC). Both trench walls show a fault zone (Fig. 12) consisting of two main, 70° dipping fault traces with vertical displacements, WSW side down, and spaced 1 m apart. The fault zone is aligned with the outcropping main plane of F1 (Fig. 1d, red line in Fig. 3) and is oriented N160°–N165° perpendicular to the stream incision (Fig. 11). Three additional faults are on the downthrown side (metre 7–11). The characteristics of the AC deposits on the walls at the northern edge of the excavation (i.e. backtilting of layers, pebbly and wedge texture) suggest the presence of another fault scarp several metres towards the NE (possibly the other plane of the F1 zone, marked with green line in Fig. 3).

Our analysis of the stratigraphic and structural setting infers three distinct earthquakes on both walls, with E1, E2 and E3 listed as oldest to youngest. The event horizons are set by the presence of faulted colluvial wedges (CW) at different depths, upward terminating faults, tilting, and channel offsets. The most recent event, E3, is uncertain, lacking unequivocal evidence. Uncertainties related to channelling and slope deposition affect our determination of vertical offsets; however, the thickness of the CW suggests a vertical offsets per event E1 and E2 larger than 0.6 m. Following Wells & Coppersmith (1994), this estimate is consistent with an earthquake with $M \gg 6$. An unknown number of older earthquakes (En) occurred along the main faults producing a minimum 2-m-high scarp (thickness of FDc at the fault zone). The cumulative vertical dislocation juxtaposes the strongly cemented conglomerate of the fan delta sequence (FD) with conglomerate in the hangingwall, resulting from its erosion (FDc). We used 14C to date 12 samples. Among these, we discarded those ages that clearly were out of sequence due to reworking of charcoals and plant material contamination, commonly

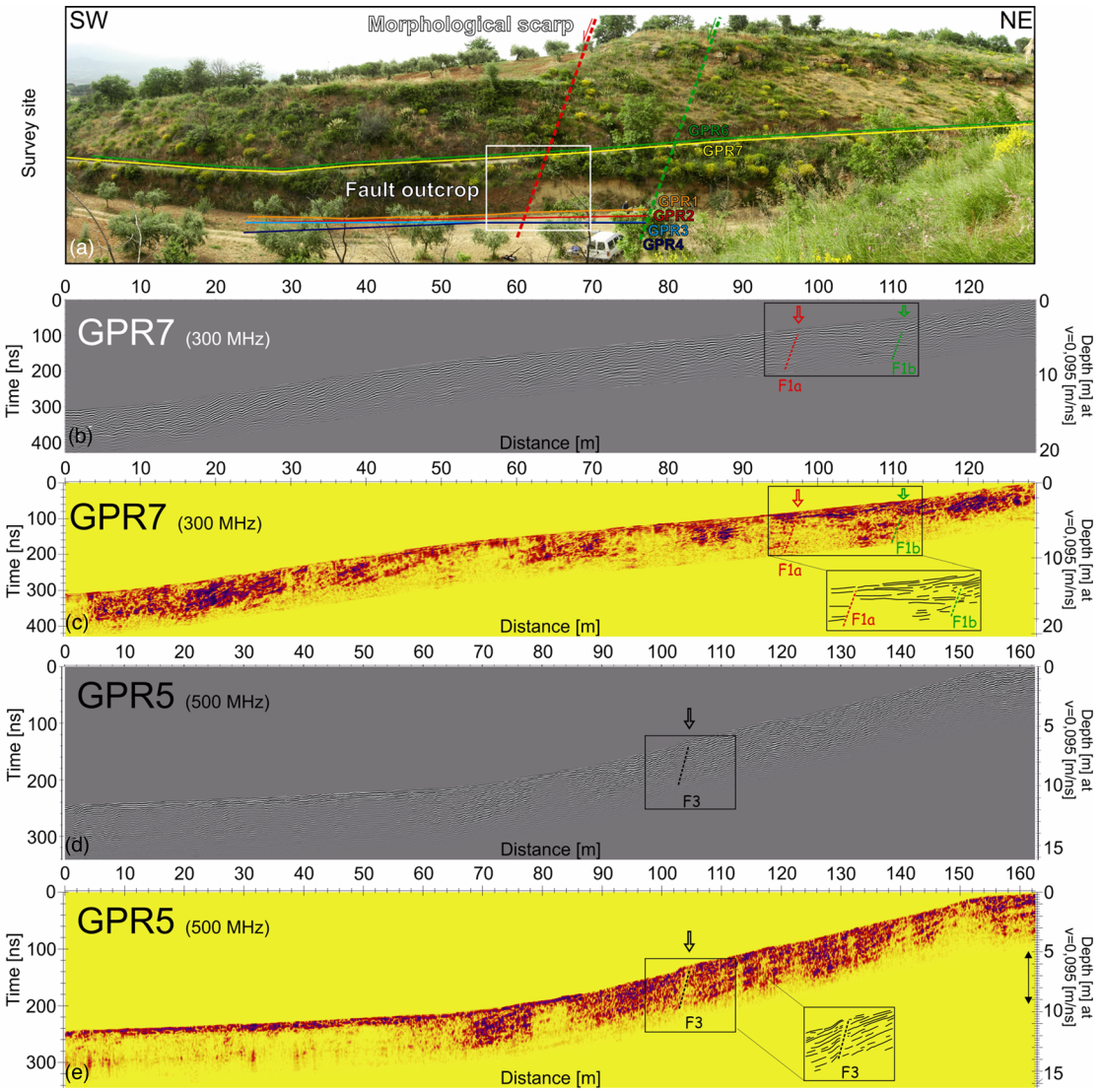

Figure 9. (a) Panorama picture of the survey site, showing the 2-D GPR1, 2, 3 and 4 profiles (orange, red, cyan and blue lines) and GPR7 (yellow line). See also Fig. 1(c) for location. GPR7 profiles (b) fully-processed and (c) image obtained by overlapping instantaneous amplitude and phase attributes. GPR5 profiles (d) and (e) after the same treatment (location in Fig. 1c). Red, green and black dotted lines are the interpreted fault zones. Vertical exaggeration is 2.

occurring in this depositional environment. Samples from the upper portion of the AC deposits of the southern wall are crossed by veins of sand from the overlying reworked material, and the resulting younger ages, with respect to those in the northern wall, could be also due to contamination. However, the 2 sigma intervals ages (Fig. 12) and the inferred event horizons (stars in Fig. 12) suggest the following timing of the recognized events: the most recent (the uncertain E3) occurred around 1200–1300 A.D., the second event (E2) between the 348 A.D. and 1185 A.D. (possibly around 500 A.D.), the third event (E1) is older than 348 A.D., but the exact age is unknown. None of these large earthquakes are included in the historical seismicity catalogues for the area.

If we merge the palaeoseismic data from our work with those collected at different sections of the Cfs (Cinti *et al.* 1997, 2002), we may robustly determine that the vertical slip per event produced by the Cf palaeoearthquakes varies along a rough N–S to NNW–SSE strike, with between 0.8 and 1.6 m on the central portion of the fault scarp system in Fig. 1(a), 0.4–0.5 m close to the northern tip in proximity of the Pollino range, and a minimum of 0.6 m on the southern portion (this study site, Figs 1a and b). At multiple sites, robust data suggest a surface faulting earthquake along the Cfs after the V–VI century A.D. but before the X century A.D., with the older part of the interval preferred (around 500 A.D.).

We observe a 2-m-minimum vertical offset produced by En events at least in the last 3300 yr (oldest age available in the trench wall stratigraphy, unit FDc). This suggests a short-term maximum slip rate of ∼0.6 mm yr^{-1}. This estimate is apparently higher than the long-term minimum value of ∼0.3 mm yr^{-1} at the site (see Section 1). This discrepancy in slip rates might simply result from our uncertainties on the ages of the displaced deposits; we have insufficient data to resolve if continuous surface faulting occurred with fairly constant average slip rates since late Pleistocene or if the slip on the F1 fault zone has increased in the recent time.

4 DISCUSSION AND CONCLUSION

The analysis of multiple closely spaced data sets allows us to integrate the stratigraphy, the fault locations, and the vertical offsets. Our multidisciplinary and multiscale approach for imaging the Cf

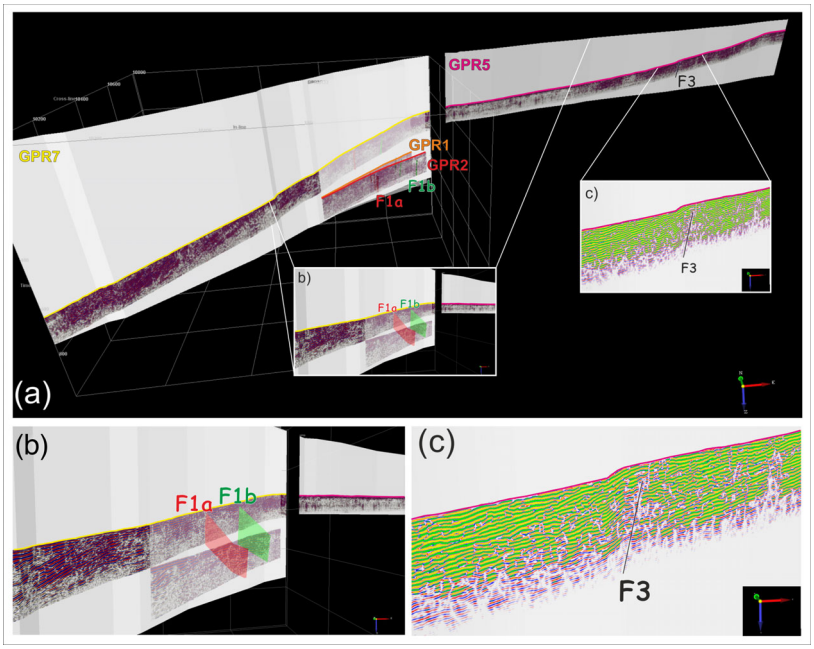

Figure 10. 3-D perspective of profiles GPR 1, 2, 5 and 7 (for locations see Fig. 1c). Three main fault strands are recognized (red, green and black). (a) Global view. (b) Details of F1 fault zone. (c) Detail of fault strand F3. The fault and layers visualization has been enhanced by using a green colour palette.

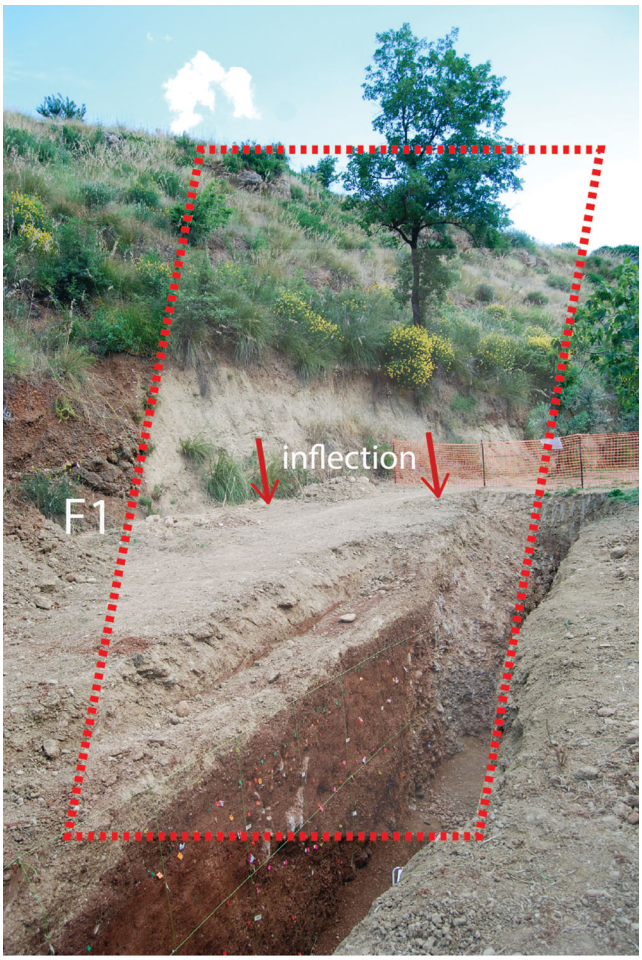

Figure 11. View of the excavation about 6 m from the northern edge of the valley, where F1 fault zone outcrops (see location in Fig. 1c). The inflection on the ground (red arrows) occurs along the main fault plane of F1 zone.

permits the recognition and characterization of complex fault geometries in plan view and in depth.

4.1 Cross-correlation of the faults location

Fig. 13 displays the locations of the faults as imaged from the different methodologies at the Rocchino site, where we used geomorphological analysis (squares), ERT survey (stars), GPR surveys (circles) and trenching (triangles). In Fig. 13, symbols are depicted with 'X' when the data are uncertain, and the locations of outcrops containing the F1 main fault and the F2 fault are shown.

Despite the varying resolutions of the techniques used in this study, each data set independently reveals the presence of four fault planes at approximately the same location at the surface. In particular, the faults outlined in red (F1) and green (F2) are well constrained by all the applied techniques (Fig. 13). Uncertainty remains for correlations among the northeastern points (black points), although at least one fault plane, F3, is well constrained from GPR and geomorphological data.

We acquire 37 fault data points in our study area (∼1 point/2200 m^2) which allow us to evaluate the slip history of the Castrovillari scarp. The fault array trended 220 m along the strike of the Cfs within a 370-m-wide zone. We identify four sub-parallel zones striking, on average, about N146°.

The mismatch between the fault trace, inferred from geomorphological analysis (squares) and from the geophysical data, is systematic for the four fault traces and is reasonably due to the differences in elevations at the respective acquisition sites (see next section).

The shallow subsurface imaging techniques are particularly useful in the accurate positioning of the fault planes where erosional/depositional/anthropic processes have modified the scarps, such as within stream valleys and urbanized zones.

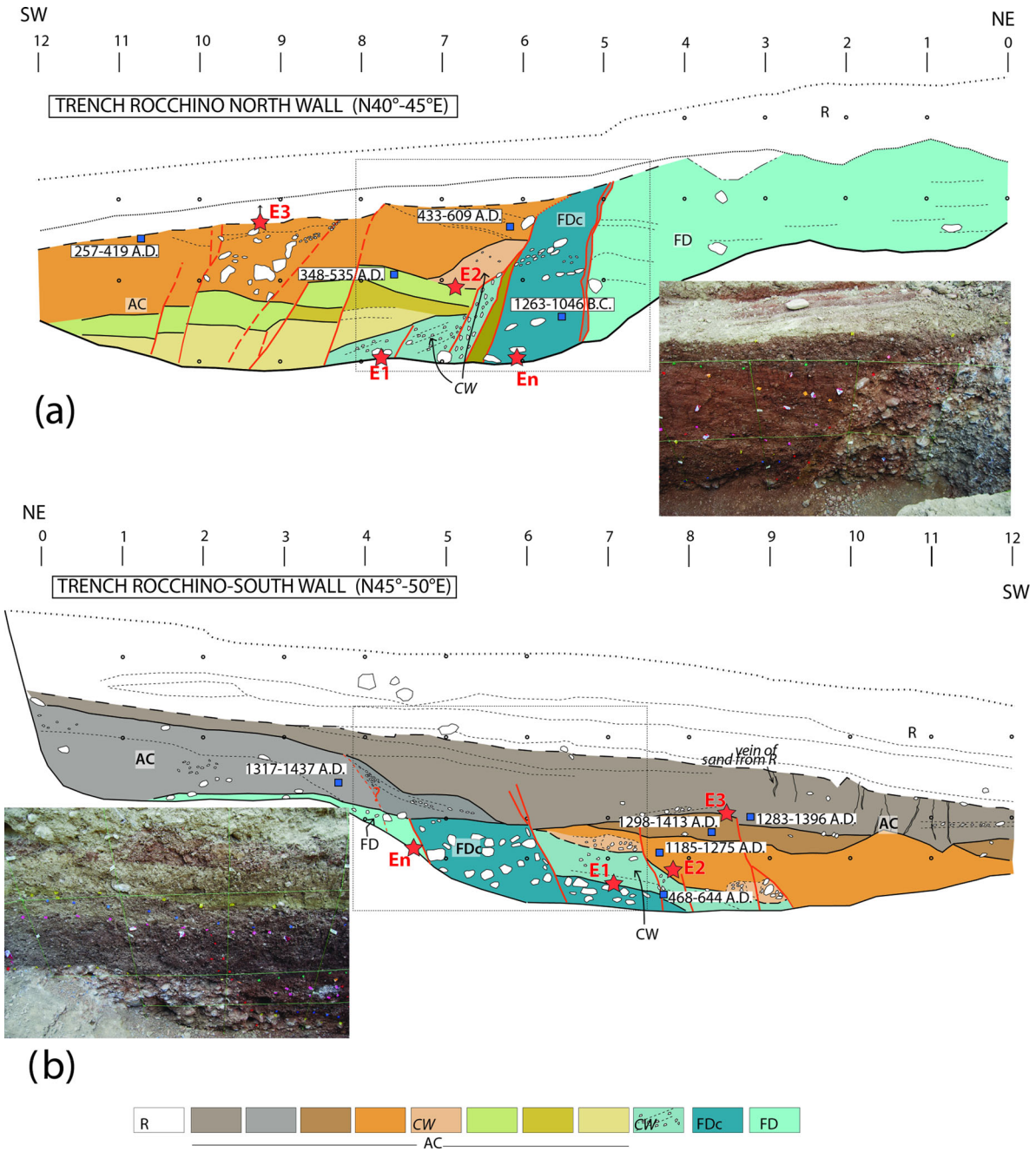

Figure 12. Log of the trench walls (horizontal versus vertical ratio 1:1, distances are in metres) and views of the main fault zones (dashed box in the logs includes the metres shown). (a) Northern wall. (b) Southern wall. The fault planes are represented with red lines. The sedimentary sequence is distinguished by main units and subunits with different colours: from the youngest to the oldest, R – reworked material; AC – alluvium and colluvium deposits; CW – colluvium wedge; FDc – conglomerate from FD erosion; FD – (fan delta) conglomerate. 14C ages (2σ interval) of the dated samples are reported. Red stars are positioned on the inferred event horizons of En to E3 events.

4.2 Depth correlation of faults geometry and displacements

We infer the geometry of the fault planes at depth by merging the location, position, and elevation of each data point. Focusing on the resolved fault locations (F1, red and green points in Fig. 13), we estimate the dip for both traces of the fault zone. Using the elevation difference between the fault points, as determined from geomorphic analysis versus subsurface data (max depth detected around 20 m) and their linear distance, we estimate an approximate southwest dip of 70°–75° for the red plane and a slightly lower dip of 65° for the green plane. Although we have fewer available data points, we infer a steeper dip (75°–80°) for F2 plane (blue). Despite the uncertainties affecting the DEM resolution and the point locations, our estimated dip values are comparable with those measured in outcrop and imaged by geophysics at specific points along the plane (F1 main fault around 70°; Figs 1d, 4 and 8). In particular, the reconstructed geometry of the F1 zone is consistent with the GPR profiles, which image the green plane to 7 m depth, dipping slightly less than the southern red plane (Figs 8 and 9). The 3-D schematic reconstruction of the two closely spaced planes of the F1 zone is

Figure 13. Plan view of the study area and fault locations inferred from various investigative techniques. Each fault location is marked with the same colour. Red and green represent faults F1, blue represents fault F2, and black represents fault F3. The satellite photograph is from Esri imagery service.

shown in Fig. 14. Assuming constant dips, the northeastern fault splay (green) joins the main fault F1 (red) at about 200 m below the topographic surface. At greater depths, the fault consists of a single plane. However, the maximum seismogenetic depth of such a fault plane remains unknown.

The resulting fault array (F1 zone, F2 and F3) indicates the complexity of the Cf at shallow depth, where the displacement appears concentrated along three main fault planes. Being its surface expression almost completely eroded over time, it is likely that F3 is the oldest splay, and is no longer active. The F1 planes exhibit the larger displacements (between 8 and 12 m). The F1 zone displaces Holocene alluvial deposits within the valley floor, and the repeated slip has influenced the morphology of the valley, as discussed in the Section 3.1. We do not have absolute data on the timing of slip on the F1 and F2 faults. However, the evidence collected supports our hypothesis that the F1 fault planes have accommodated most of the deformation at the Rocchino site.

Finally, our data confirm the presence of a seismogenic fault in the Castrovillari area. This fault is able to produce $M > 6$ earthquakes with complex, multiple ruptures at surface. Therefore, the seismic assessment of this area should include surface faulting hazard studies devoted to improve the urban and infrastructure planning activities.

ACKNOWLEDGEMENTS

Special thanks to Mr Rocco (alias Rocchino) for his kindness and allowing trenching on his private land. We are grateful to Comandante Giorgio Papaianni of the Corpo Forestale dello Stato, Stazione di Civita, for logistical support and kind availability. Leonardo Speziali is acknowledged for his useful help during the field data acquisition. Many thanks also to anyone occasionally involved during the survey. We are indebted to the reviewers for the detailed and insightful

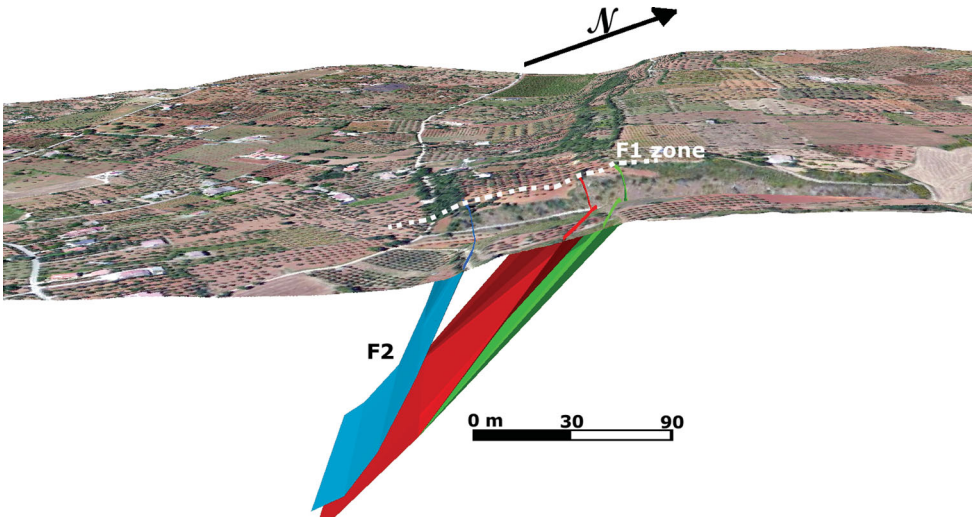

Figure 14. 3-D sketch (view to the north) of the main faults planes as inferred from near-surface data at the Rocchino site (vertical versus horizontal distances 3:1). The white dashed line marks the slope of the Cfs at the site.

comments that substantially improved the clarity of the paper. This study has benefited from funding provided by the Italian Presidenza del Consiglio dei Ministri - Dipartimento della Protezione Civile (DPC). This paper does not necessarily represent DPC official opinion and policies.

Co-authors from INGV carried out the geomorphological and trenching data and analysis, those from the Dipartimento di Scienza e Alta Tecnologia of the Insubria performed the ERT survey and data elaboration, and those from the Dipartimento di Fisica e Geologia of Perugia performed the GPR survey and data elaboration.

Source of aerial view of Figs 1(c), 2, 13 and 14 is from Esri, DigitalGlobe, GeoEye, i-cubed, Earthstar Geographics, CNES/Airbus DS, USDA, USGS, AEX, Getmapping, Aerogrid, IGN, IGP, swisstopo and the GIS User Community.

REFERENCES

Bousquet, J.C., 1973. La tectonique recente de l'Apennin Calabro-Lucanien dans son cadre geologique et geophysique, *Geologica Romana,* **12,** 1–104 (in French).

Brunori, C.A., Civico, R., Cinti, F.R. & Ventura, G., 2013. Characterization of active fault scarps from LiDAR data: a case study from central Apennines (Italy), *Int. J. Geogr. Inf. Sci.,* **27**(7), doi:10.1080/13658816.2012.684385.

Carpentier, S.F.A., Green, A.G., Doetsch, J., Dorn, C., Kaiser, A.E., Campbell, F., Horstmeyer, H. & Finnemore, M., 2012. Recent deformation of quaternary sediments as inferred from GPR images and shallow *P*-wave velocity tomograms: Northwest Canterbury Plains, New Zealand, *J. appl. Geophys.,* **81,** 2–15.

Christie, M., Tsoflias, G.P., Stockli, D.F. & Black, R., 2009. Assessing fault displacement and off-fault deformation in an extensional tectonic setting using 3-D ground penetrating radar imaging, *J. appl. Geophys.,* **68**(1), 9–16.

Cinti, F.R., Cucci, L., Pantosti, D., D'Addezio, G. & Meghraoui, M., 1997. A major seismogenic fault in a 'silent area': The Castrovillari fault (southern Apennines, Italy), *Geophys. J. Int.,* **130,** 595–605.

Cinti, F.R., Moro, M., Pantosti, D., Cucci, L. & D'addezio, G. 2002. New constraints on the seismic history of the Castrovillari fault in the Pollino gap (Calabria, southern Italy), *J. Seismol.,* **6,** 199–217.

Cinti, F.R., Alfonsi, L., D'Alessio, A., Marino, S. & Brunori, C.A., 2015. Faulting and Ancient Earthquakes at Sybaris Archaeological Site, Ionian Calabria, Southern Italy, *Seism. Res. Lett.,* **86**(1), doi:10.1785/02201401071.

Colella, A., 1994. Coarse-grained deltas in neotectonic strike-slip and extensional settings: tectonic and sedimentary controls on the architecture of deltas and basin fills (Crati basin and Messina Straits, southern Italy), in *Proceedings of the 15th Int.* Ass. Sedim. Regional Meeting, Ischia, Italy, pp. 247–277.

Ercoli, M., Pauselli, C., Frigeri, A., Forte, E. & Federico, C., 2013. Geophysical paleoseismology through high resolution GPR data: a case of shallow faulting imaging in Central Italy, *J. appl. Geophys.,* **90,** 27–40.

Ercoli, M., Pauselli, C., Frigeri, A., Forte, E. & Federico, C., 2014. 3-D GPR data analysis for high resolution imaging of shallow subsurface faults: the Mt. Vettore case study (Central Apennines, Italy), *Geophys. J. Int.,* **198,** 609–621.

Italian Seismological Instrumental and Parametric Database [ISIDe] Working Group, 2010. Italian seismological instrumental and parametric database, Available at: http://iside.rm.ingv.it, last accessed 20 September 2015.

Jewell, C.J. & Bristow, C.S., 2006. GPR studies in the Piano di Pezza area of the Ovindoli–Pezza Fault, Central Apennines, Italy: extending paleoseismic trench investigations with high resolution GPR profiling, *Near Surf. Geophys.,* **4**(3), 147–153.

Jol, H.M., 2009. *Ground Penetrating Radar Theory and Applications,* Elsevier Ltd.

Liner, C.L. & Liner, J.L., 1997. Application of GPR to a site investigation involving shallow faults, *Leading Edge,* **16**(11), 1649–1651.

Loke, M.H., 2011. Electrical resistivity surveys and data interpretation, in *Solid Earth Geophysics Encyclopaedia,* 2nd edn: *Electrical & Electromagnetic*, pp. 276–283, ed. Gupta, H, Springer-Verlag.

McClymont, A.F., Green, A.G., Kaiser, A., Horstmeyer, H. & Langridge, R., 2010. Shallow fault segmentation of the Alpine fault zone, New Zealand revealed from 2- and 3-D GPR surveying, *J. appl. Geophys.,* **70**(4), 343–354.

Michetti, A.M., Ferreli, L., Serva, L. & Vittori, E., 1997. Geological evidence for strong historical earthquakes in an "aseismic" region: the Pollino case (southern Italy), *J. Geodyn*. **24**(1/4), 61–86.

Michetti, A.M., Ferreli, L., Esposito, E., Porfido, S., Blumetti, A.M., Vittori, E., Serva, L. & Roberts, G.P., 2000. Ground effects during the 9 September 1998, Mw = 5.6 Lauria earthquake and the seismic potential of the "aseismic" Pollino Region in Southern Italy, *Seism. Res. Lett.,* **71**(1), 31–46.

Pauselli, C., Federico, C., Frigeri, A., Orosei, R., Barchi, M.R. & Basile, G., 2010. Ground penetrating radar investigations to study active faults in the Norcia Basin (Central Italy), *J. appl. Geophys.,* **72,** 39–45.

Rovida, A., Camassi, R., Gasperini, P. & Stucchi, M. (a cura di), 2011. CPTI11, la versione 2011 del Catalogo Parametrico dei Terremoti Italiani, Milano, Bologna, Available at: http://emidius.mi.ingv.it/ CPTI, last accessed March 2014, doi:10.6092/INGV.IT-CPTI11.

Russo, F. & Schiattarella, M., 1992. Osservazioni preliminari sull'evoluzione morfostrutturale del bacino di Castrovillari, *Studi Geologici Camerti,* **1992/1,** 271–278 (in Italian).

Tertulliani, A. & Cucci, L. 2014. New insights on the strongest historical earthquake in the Pollino Region (Southern Italy), *Seismol. Res. Lett.,* **85**(3), 743–751.

Vanneste, K., Verbeeck, K. & Petermans, T., 2008. Pseudo-3-D imaging of a low-slip-rate, active normal fault using shallow geophysical methods: the Geleen fault in the Belgian Mass River valley, *Geophysics,* **73**(1), B1–B9.

Wells, D.L. & Coppersmith, K.J., 1994. New empirical relationships among magnitude, rupture length, rupture width, rupture area, and surface displacement, *Bull. seism. Soc. Am.,* **84,** 974–1002.

Zhao, W., Forte, E., Pipan, M. & Tian, G., 2013. Ground penetrating radar (GPR) attribute analysis for archaeological prospection, *J. appl. Geophys.,* **97,** 107–117.